Polymer Chemistry

RSC Publishing

PAPER

View Article Online
View Journal | View Issue

Cite this: *Polym. Chem.*, 2013, **4**, 3411

Fluorinated thienyl-quinoxaline-based D–π–A-type copolymer toward efficient polymer solar cells: synthesis, characterization, and photovoltaic properties†

Hsieh-Chih Chen,*[ab] Ying-Hsiao Chen,[ab] Chung-Hao Liu,[c] Yen-Hao Hsu,[a] Yun-Chen Chien,[a] Wei-Ti Chuang,[ab] Chih-Yang Cheng,[c] Chien-Liang Liu,[ab] Shang-Wei Chou,[ab] Shih-Huang Tung*[bc] and Pi-Tai Chou*[ab]

A tailor-made donor–π–acceptor copolymer comprising of a medium electron-donating alkylthienyl-benzodithiophene (BDTT) moiety and a strong electron-accepting fluorinated thienyl-quinoxaline (TTFQ) segment with thiophene π-bridge units has been synthesized by Stille coupling polymerization and thoroughly characterized for use as a p-type semiconducting polymer. The semicrystalline copolymer PBDTT-TTFQ shows a broad visible-near-infrared absorption band with an optical bandgap of 1.67 eV and possesses a relatively low-lying HOMO level at −5.34 eV. In addition, the PBDTT-TTFQ neat film reveals a highly dense fibrillar nanostructure with a certain degree of long-range order, suggesting the nanoscale self-assembly of PBDTT and TTFQ segments. A bulk-heterojunction polymer solar cell based on the blend of 1 : 1 PBDTT-TTFQ:$PC_{71}BM$ shows an open circuit voltage of 0.75 V, a short circuit current density of 14.6 mA cm^{-2}, and a fill factor of 56.1%, achieving a power conversion efficiency of 6.1% under the illumination of AM 1.5G, 100 mW cm^{-2}. The results unambiguously indicate that the PBDTT-TTFQ is an auspicious candidate for next-generation solar cell materials.

Received 15th February 2013
Accepted 19th March 2013

DOI: 10.1039/c3py00235g

www.rsc.org/polymers

Introduction

In recent years, polymer solar cells (PSCs) have drawn considerable promise as renewable energy sources owing to their advantages in low-cost, lightweight, and good-flexibility for sustainable solar energy conversion.[1,2] Nowadays, the most efficient architecture of PSCs is a bulk-heterojunction (BHJ) structure with a three-dimensional interpenetrating network of conjugated polymers blended with soluble fullerene derivatives[1–17] or nanocrystals.[18–22] Recent advances in the development of novel tailor-made materials, mostly low bandgap copolymers of alternating electron-rich (donor, D) and electron-poor (acceptor, A) repeat unit configurations, have brought about great improvements in device performances. The D–A intramolecular charge transfer (ICT) within the backbone repeat unit allows facile reduction of the bandgaps, fine-tuning of the frontier molecular orbital energies, and harvesting of light absorption toward longer wavelengths.[1,2] In addition, highly extended π-conjugated polymers also benefit from ordered or crystalline domains to promote strong face-to-face π–π stacking of the conjugated backbones, resulting in higher charge-carrier mobility and broadening of the absorption bands relative to the lower homologues.[5,23–25] Recently, significant progress has been made in this field, and the power conversion efficiencies (PCEs) of PSCs have reached 7–8%,[3–10] primarily because of the development of new low-bandgap polymers and better control over the nanoscale morphologies of interpenetrating electron D–A networks.

Benzo[1,2-*b*:4,5-*b*′]-dithiophene (BDT), as one of the most successful electron donor units, has emerged as an attractive building block for PSCs due to its rigidity, coplanarity by fusing a benzene with two flanking thiophene units, high hole mobility, extended π-conjugated structures, and proper side chain patterns for enhanced solubility.[26,27] Very recently, *via* replacing the alkoxy-substitutes attached to the BDT-based D–A copolymer with alkylthienyl groups, Hou *et al.*[5] were capable of constructing a two-dimensional (2-D) conjugated BDT-polymer possessing a broader absorption band, a lower highest occupied molecular orbital (HOMO) energy level, a higher hole mobility,

[a]*Department of Chemistry, National Taiwan University, Taipei, 106, Taiwan. E-mail: austinchen@ntu.edu.tw; chop@ntu.edu.tw; Fax: +886 2 2369 5208; Tel: +886 2 3366 3894*

[b]*Center of Emerging Material and Advanced Devices, National Taiwan University, Taipei, 106, Taiwan*

[c]*Institute of Polymer Science and Engineering, National Taiwan University, Taipei, 106, Taiwan. E-mail: shtung@ntu.edu.tw; Fax: +886 2 3366 5237; Tel: +886 2 3366 5319*

† Electronic supplementary information (ESI) available: Synthesis details, device fabrication procedures, current–voltage measurements, cyclic voltammogram, UV-vis spectra, and 2-D grazing incidence X-ray scattering patterns. See DOI: 10.1039/c3py00235g

as well as a better photovoltaic efficiency than that of the alkoxy-substituted analogues. In a relevant contribution, we reported a new alternating copolymer PBDT-TFQ containing an alkoxy-substituted-BDT moiety, and a fluorinated quinoxaline (TFQ) unit as the D and the A, respectively, which was then applied in organic photovoltaic devices (OPVs) with power conversion efficiencies (PCEs) up to 8%.[3] This result indicates that TFQ is one of the efficacious acceptor units for organic semiconductors because of its strong electron affinity that offers deep HOMO energy levels and a broad absorption range, which are important parameters for p-type semiconducting polymers.[3] However, one of the main bottlenecks for the PBDT-TFQ is its relatively short absorption coverage at the near-infrared (NIR) region due to the fact that the TFQ moiety possesses a high content of benzene rings. The high aromaticity and hence the great stabilization energy of phenyl substitution leads to a relatively larger optical bandgap that limits light-harvesting. This drawback may be crucial, which motivated us to further replace the phenyl substitutions of the TFQ core with thienyl substitutions in an aim to achieve better sunlight harvesting. This is simply due to the fact that sulfur is a softer atom (*cf.* the carbon atom) so that thienyl substitution is expected to enhance the π-conjugation.

In this context, we report herein a facile and straightforward synthetic methodology to prepare a novel semi-crystalline fluorinated thienyl-quinoxaline-based D–A alternating copolymer with thiophene π-bridge units, namely, poly{4,8-bis(5-(2-ethylhexyl)thiophen-2-yl)benzo[1,2-*b*:4,5-*b*′]dithiophene-2,6-diyl-alt-[5,8-bis(5′-thiophen-2′-yl)-6,7-difluoro-2,3-bis(5-hexylthiophen-2-yl)quinoxaline-5,5′-diyl]} (PBDT-TTFQ, see Scheme 1), by Stille coupling polymerization reactions, which turns out to be a very promising candidate for efficient PSCs. This low bandgap polymer, designed based on the intrachain D–A copolymer motif, was capable of extending the absorption into the red and NIR region with the desired deep HOMO and lowest unoccupied molecular orbital (LUMO) energy levels, and also exhibited a higher hole mobility. As a result, the PSC fabricated under a blend ratio of 1 : 1 PBDTT-TTFQ:$PC_{71}BM$ attained an open-circuit voltage (V_{oc}) of 0.75 V, a short-circuit current density (J_{sc}) exceeding 14 mA cm^{-2}, a PCE of as high as 6.1%, demonstrating that the fluorinated thienyl-quinoxaline segment is a promising building block for the development of semiconducting polymers with high photovoltaic efficiency.

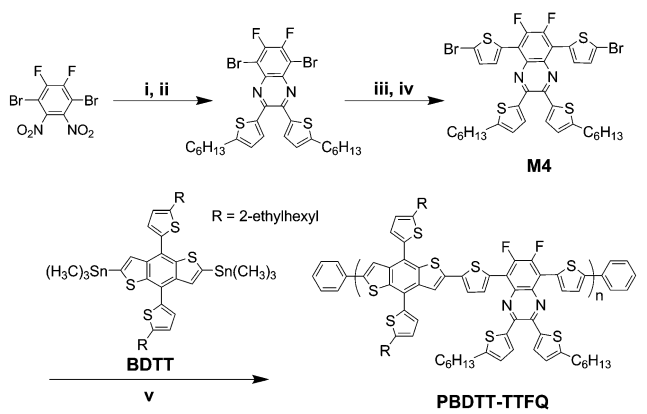

Scheme 1 Synthetic route adopted for the preparation of the PBDTT-TTFQ copolymer. The reagents and conditions: (i) Fe, AcOH, 50 °C, 4 h; (ii) 1,2-bis-(5-hexylthiophen-2-yl)ethane-1,2-dione, AcOH, reflux, overnight; (iii) 2-(tributylstannyl)thiophene, $PdCl_2(PPh_3)_2$, toluene, reflux, 24 h; (iv) NBS, DMF, 30 °C, 8 h; (v) $Pd(PPh_3)_4$, toluene, reflux, 72 h.

Experimental section

Measurement and characterization

^1H, ^{13}C, and ^{19}F NMR spectra were recorded on a Varian Mercury 400. Mass spectra were obtained on a FINNIGAN LCQ mass spectrometer. Chemical shifts (δ), quoted in parts per million (ppm), and coupling constants (J) were recorded in Hertz (Hz). All NMR spectra were recorded in deuterated chloroform or 1,1,2,2-tetrachloroethane ($CDCl_3$ or $C_2D_2Cl_4$) with solvent containing 0.003% TMS as an internal reference. The molecular weight and molecular weight distribution of the synthesized polymers were measured with a Waters GPC (Breeze system) using THF as an eluent at 35 °C. The apparatus was equipped with two Waters Styragel columns (HR3 and HR4E), a refractive index detector (Waters 2414), and a dual-wavelength absorbance detector (Waters 2487). Polystyrene standards (Waters) were used for calibration. Cyclic voltammetry (CV) was performed on an Autolab PGSTAT 30 Electrochemical Workstation with a three-electrode system in a solution of 0.1 M tetrabutylammonium perchlorate (Bu_4NClO_4) in deoxygenated acetonitrile (CH_3CN) at a scan rate of 50 mV s^{-1}. The polymer films were coated on ITO sheet working electrodes by solvent casting. A Pt-wire was used as the counter electrode, and an Ag-wire was used as a quasi-reference electrode. The HOMO level of the polymer was calculated from the onset potential of oxidation (E_{ox}^{onset}) by assuming the absolute energy level of ferrocene at −4.8 eV below the vacuum level; the LUMO level was calculated from the HOMO energy level and the absorption edge.[3] The potential of the polymer was corrected in the standard of Fc/Fc^+ in CH_3CN (0.45 V *vs.* Ag/Ag^+ electrode). Thermogravimetric analysis (TGA) and differential scanning calorimetry (DSC) measurements were performed under a nitrogen atmosphere at heating rates of 10 and 5 °C min^{-1} using a TA Instruments (TGA-951 and DSC-910S, respectively). Tapping mode atom force microscopy (TM-AFM) images were taken on a NanoScope IIIa controller (Veeco Metrology Group/Digital Instruments, Santa Barbara, CA), using built-in software (version V6.13R1) to capture images. The TEM images were obtained by JEOL JEM-1230 and Philips/FEI Tecnai 20 G^2 S-Twin transmission electron microscopes. Grazing incidence wide-angle X-ray scattering (GIWAXS) measurements were conducted at the BL23A1 endstation of the National Synchrotron Radiation Research Center (NSRRC), Taiwan. The thin films for characterization were deposited on a 1 cm × 2 cm silicon wafer. A monochromatic beam of wavelength $\lambda = 0.826$ Å (15 keV) was used and the incident angle was 0.2°. The scattering patterns were collected on a CMOS flat panel X-ray detector C9728DK (52.8 mm × 52.8 mm). The scattering intensity profiles were extracted from the 2D patterns and reported as the plots of the scattering intensity I *vs.* the scattering vector q, where $q = (4\pi/\lambda)$

sin(θ/2) and θ is the scattering angle. The absorption spectra were obtained on a Hitachi U-4100 spectrophotometer. Hole-only devices were fabricated according to a similar method described in the literature,[37,38] using a diode configuration of ITO/PEDOT:PSS/polymer:$PC_{71}BM$/Pd (80 nm). Electron-only devices were fabricated with a diode configuration of ITO/Al (50 nm)/polymer:$PC_{71}BM$/Al (100 nm). The SCLC current was measured under dark conditions using a Keithley 4200 Source Meter.

Solar cell device fabrication and characterization

Optimized solar cell devices used in this study were prepared by dissolving PBDTT-TTFQ and $PC_{71}BM$ (purchased from Nano-C) in 1,2-dichlorobenzene (DCB) in the weight ratios of 1 : 1, and 1 : 2 with a PBDTT-TTFQ concentration of 10 mg mL^{-1}. For device fabrication, the solution was stirred for more than 12 h to ensure complete dissolution. Patterned indium tin oxide (ITO)-coated glass substrates (Kintec Company, 15 Ω per □) were successively cleaned by ultrasonication in 1% neutral detergent in water, followed by deionized water, then acetone, and finally ethanol for 20 min each. The substrates were then dried and O_2 plasma cleaned immediately prior to the deposition of a 35 nm thick layer of aqueous PEDOT:PSS PH500 (H. C. Starck) solution, as verified by a Filmetrics Model F10-RT-UV system. Deposition of the PEDOT:PSS layer was followed by baking at 140 °C for 20 min. Substrates were subsequently transferred to an inert N_2-filled glove box (<0.1 ppm O_2 and H_2O), and the active layer was spin-coated. The wet film was slowly dried in a covered Petri dish for a certain time and subsequently annealed at 150 °C for 10 min in the glove box. The thicknesses of the PBDTT-TTFQ:$PC_{71}BM$ composite films were adjusted to ~100 to 130 nm by controlling the spin-coating rates. The coated substrates were then transferred to a thermal evaporator and evacuated to $\leq 1 \times 10^{-6}$ Torr before a 30 nm thick calcium layer followed by a 100 nm aluminum electrode layer were deposited. The effective area of one cell was 0.04 cm^2. The fabricated device was encapsulated in a nitrogen-filled glove box with UV epoxy and cover glass. The *J–V* curves were measured with a Newport-Oriel (Sol3A Class AAA Solar Simulators) AM 1.5G light source operating at 100 mW cm^{-2}, and independently cross-checked using a 300 W AM 1.5G source operating at 100 mW cm^{-2} for verification. The light intensity was determined by a mono-silicon detector (with KG-5 visible color filter) calibrated by the National Renewable Energy Laboratory (NREL) to minimize spectral mismatch. An IPCE (QE10) characterization platform supplied by PV Measurement, Inc. was used for data acquisition. All IPCE spectra were recorded using a lock-in technique at a chopping frequency of 100 Hz.

Results and discussion

On the basis of the D–A concept, the medium electron-donating BDTT moiety and strong electron-accepting TTFQ unit were utilized to synthesize the low bandgap PBDTT-TTFQ copolymer. The brief synthetic routes of monomers and the corresponding polymer are illustrated in Scheme 1. PBDTT-TTFQ was synthesized in good yield through a Stille coupling reaction using $Pd(PPh_3)_4$ as a catalyst *via* thermal heating shown in the ESI.† The crude polymer was precipitated into methanol and filtered, followed by careful extraction with methanol, acetone, dichloromethane and chloroform with Soxhlet apparatus to remove byproducts and oligomers. The final product was obtained from the chloroform fraction precipitated into methanol, filtered and dried under vacuum for 12 h. PBDTT-TTFQ exhibits an excellent film-casting property as well as good solubility in common halogenated solvents. The number-average molecular weight (M_n) of the synthesized copolymer PBDTT-TTFQ was determined by gel permeation chromatography (GPC) using a polystyrene standard in THF eluent, and was found to be 43 kg mol^{-1} with a polydispersity index (PDI) of 1.58.

The thermal stability of the copolymer was confirmed by thermogravimetric analysis (TGA) at a temperature ramp rate of 10 °C min^{-1} under nitrogen atmosphere. The onset decomposition temperature of PBDTT-TTFQ at 5% weight loss is 405 °C, indicating high thermal stability of the as-prepared polymer (see Fig. 1a). Through differential scanning calorimetry (DSC) measurements, PBDTT-TTFQ copolymer shows a high glass-transition temperature (T_g) of 126 °C probably because of the high chain rigidity of the polymer backbone. The optical absorption spectra of PBDTT-TTFQ acquired in 1,2-dichlorobenzene (DCB) solution and as a film are shown in Fig. 1b.

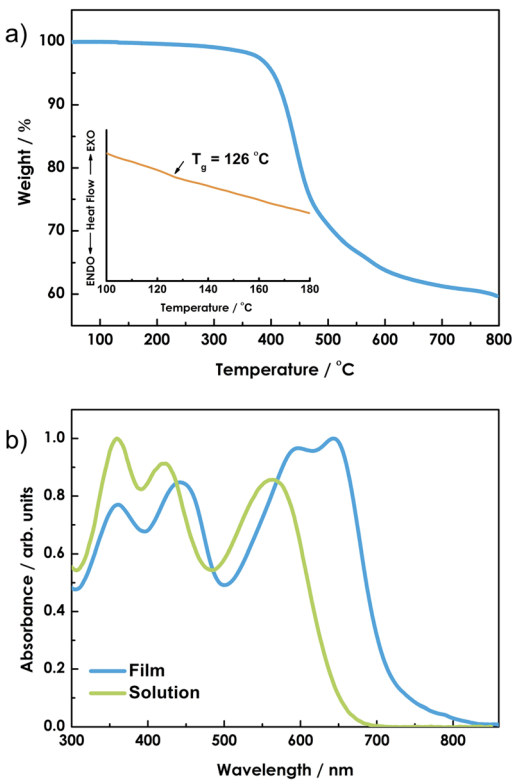

Fig. 1 (a) Thermogravimetric analysis (ramp rate: 10 °C min^{-1}) of PBDTT-TTFQ. The purge gas for TGA was nitrogen. Inset: DSC curve of the studied copolymer. (b) UV-vis absorption spectra of PBDTT-TTFQ in 1,2-dichlorobenzene solution and as a film.

PBDTT-TTFQ in dilute DCB solution exhibits a broad and strong absorption spectral feature across the entire UV-vis region, with three major absorption bands and hence peak wavelengths located at 359, 421 and 563 nm. The two higher energy bands originate from the localized π–π* transitions, whereas the lowest lying band is attributed to the ICT from the PBDTT unit to the TTFQ core. In the polymer film, the corresponding absorption becomes broader and is significantly red-shifted as compared with the corresponding maxima of the polymer solution with four peaks at 361, 441, 593 and 645 nm. The large red-shift of 30 nm is observed in the absorption maxima (λ_{max}) relative to the dilute solution as a result of a more planar polymer chain structure and/or the degree of interchain π-stacking in the solid film. Such an ordered packing of polymer chains is beneficial for improving the charge carrier mobility of the resulting films. Furthermore, the absorption edge (λ_{edge}) of PBDTT-TTFQ film is 742 nm, from which the lowest-lying energy gap E_g^{opt} of PBDTT-TTFQ, deduced from the onset of absorption in the solid state, is determined to be 1.67 eV. Detailed optical and electrochemical properties of PBDTT-TTFQ are summarized in Table 1.

Experimentally, cyclic voltammetry (CV) was employed to examine the electrochemical properties and determine the HOMO and LUMO energies of the as-prepared copolymer (see Fig. S14†). The PBDTT-TTFQ copolymer showed stable and quasi-reversible p-doping and n-doping processes, which are important prerequisites for p-type semiconductor materials. The HOMO and LUMO energy levels for PBDTT-TTFQ were found to be −5.34 and −3.26 eV, respectively. A slightly higher energy bandgap was determined using CV (2.08 eV) than that from UV-vis absorption measurements (1.67 eV). The discrepancy, on the one hand, is probably because of an energy barrier between the polymer film and electrode used in the CV measurement. On the other hand, however, the different binding energy of excitons created in the optical and electrochemical measurement cannot be eliminated. A deeply low-lying HOMO energy level was obtained for PBDTT-TTFQ, which is in an ideal range to ensure better air-stability and can be anticipated to approach high V_{oc}, in accordance with the linear correlation of the difference between the HOMO energy level of a donor polymer and the LUMO energy level of an acceptor.[28] Considering the LUMO level of $PC_{71}BM$ is located at −4.0 eV, the offset between donor polymer and acceptor $PC_{71}BM$ should provide a sufficient driving force for efficient exciton dissociation at the D–A interface, ensuring energetically favorable electron transfer.[1,2]

To provide an in-depth insight into the molecular architecture of the polymer, a molecular simulation was carried out using density functional theory (DFT) at the B3LYP/6-31G* level with the Gaussian 09 package in an aim to estimate the optimized geometries and the corresponding charge-density isosurfaces properties. The resulting frontier molecular orbitals depicted in Fig. 2 predict that the electron density of the HOMO is mainly localized at the PBDTT and in part at the benzene site of TTFQ, while the electron density of the LUMO is dominantly localized on the entire TTFQ moiety. The analysis provides sufficient evidence of the formation of a D–π–A structure and the intramolecular charge transfer (ICT) behavior of the material.

Photovoltaic properties of the PBDTT-TTFQ copolymer were investigated in solar cells with a device configuration of ITO/PEDOT:PSS/polymer:$PC_{71}BM$/Ca/Al. The asymmetric $PC_{71}BM$ was used due to its stronger light absorption in the visible region than that of $PC_{61}BM$. Fig. 3a depicts the current density–voltage (J–V) curves of the BHJ solar devices with various blend ratios of PBDTT-TTFQ:$PC_{71}BM$ measured under simulated one-sun AM1.5G illumination. It was noticed that the V_{oc} of PBDTT-TTFQ-based devices dropped from 0.75 to 0.72 V with increasing $PC_{71}BM$ content in the blends, and the device with a D–A ratio of 1 : 1 showed the highest J_{sc} in these two conditions. As reported, the device fabrication process of a PSC can be further improved by thermal annealing and/or by using 1,8-diiodooctane (DIO) as an additive owing to its high boiling point (168 °C) and ability to solvate the fullerenes during the spin-coating process.[29,30] In this work, both of these two methods (150 °C for 10 min, 3 vol% DIO) were employed to optimize the device performance. The device based on the PBDTT-TTFQ:$PC_{71}BM$ (1 : 1 in wt%) blends revealed a V_{oc} of 0.75 V, a J_{sc} of 14.6 mA cm^{-2}, a FF of 56.1%, delivering an exceptional PCE of 6.1%. Indeed, the high V_{oc} is attributed to the lower-lying HOMO energy level of PBDTT-TTFQ as a result of the fluorine electron-withdrawing effect on the TTFQ unit, and the result is in complete accord with previous reports.[3,4,7,31] The

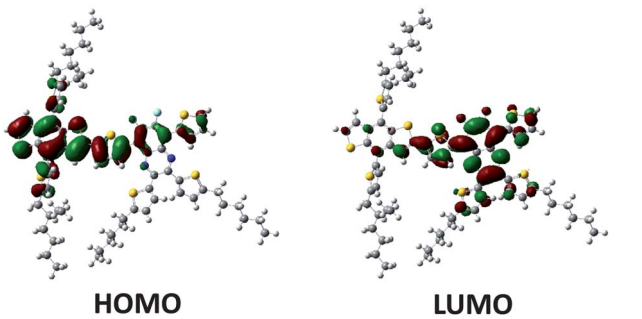

Fig. 2 DFT optimized geometries and corresponding charge-density isosurfaces for the HOMO and LUMO distributions of PBDTT-TTFQ copolymer.

Table 1 Physical, optical and electrochemical properties of the polymer

Polymer	M_n [kg mol^{-1}]	PDI	T_g [°C]	T_d [°C]	Solution/λ_{max} [nm]	Film/λ_{max} [nm]	HOMO[a] [eV]	LUMO[a] [eV]	E_g^{EC}[b] [eV]	E_g^{opt}[c] [eV]
PBDTT-TTFQ	43	1.58	126	405	359, 421, 563	361, 441, 593, 645	−5.34	−3.26	2.08	1.67

[a] HOMO and LUMO levels were estimated from the onset of the oxidation and reduction peaks of the cyclic voltammogram (CV). [b] Electrochemical bandgap calculated from the CV. [c] Optical bandgap estimated from the onset of UV-vis spectrum of the film.

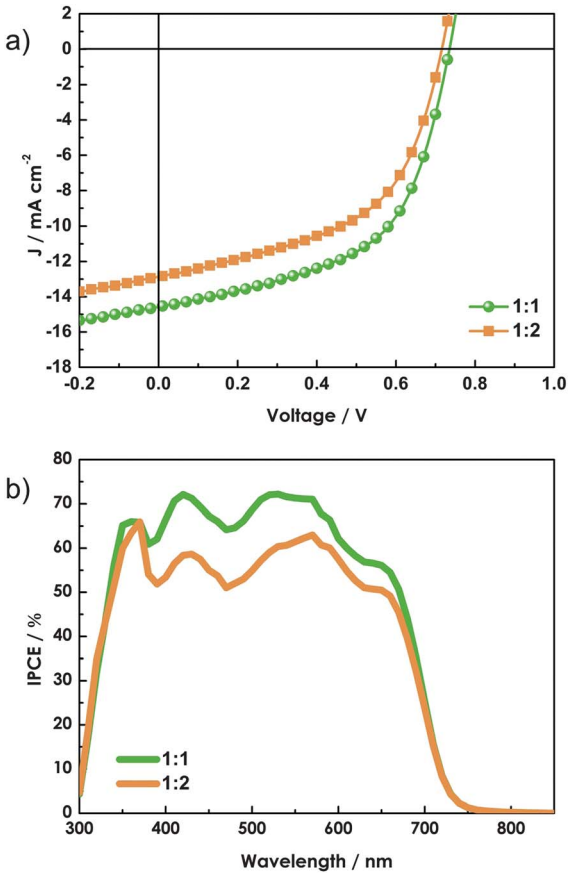

Fig. 3 (a) Current density *versus* voltage (*J–V*) characteristics of optimized devices made from different blend ratios of PBDTT-TTFQ:$PC_{71}BM$ measured under AM 1.5G solar illumination. For the 1 : 1 device (●): V_{oc} = 0.75 V, J_{sc} = −14.6 mA cm^{-2}, FF = 56.1%, and PCE = 6.1%. For the 1 : 2 device (■): V_{oc} = 0.72 V, J_{sc} = −12.8 mA cm^{-2}, FF = 52.3%, and PCE = 4.8%. (b) Corresponding IPCE spectra of the optimized devices made from different ratios of the PBDTT-TTFQ:$PC_{71}BM$ blends illuminated by monochromatic light.

introduction of fluorine substituents on D–A conjugated polymers has a minor effect on their optical properties but affects significantly their energy levels owing to its strong electronegativity. This has led to the decrease of both HOMO and LUMO energy levels, rendering higher V_{oc} values. The superior PSC performance of the 1 : 1 blends is associated with the high hole mobility and better nanoscale morphology of the interpenetrating network (*vide infra*), allowing efficient exciton dissociation and enhancing charge carrier transportation.[32–36] However, further increasing the blend ratio to 1 : 2 significantly deteriorates all photovoltaic parameters (V_{oc}, J_{sc}, and FF) and results in a lower PSC efficiency (see Fig. 3a and Table 2). To verify the accuracy of the photo *J–V* measurements, the corresponding incident photon-to-current efficiency (IPCE) spectra of the devices elaborated above were measured under illumination of monochromatic light shown in Fig. 3b. According to the PSC devices fabricated with various PBDTT-TTFQ:$PC_{71}BM$ blend ratios, very broad panchromatic spectra over the entire excitation spectral range were obtained from IPCE measurements. The optimum device very efficiently harvests solar light with the maximum IPCE of 72% at 420 nm, and exhibits a broad photoresponse of over 60% in the 343–612 nm range. Moreover, the IPCE spectra accord well with the absorption spectra of the blends (Fig. S15†), resulting in a close correlation with the photocurrents. The integral J_{sc} of both devices with blend ratios of 1 : 1 and 1 : 2 from IPCE curves are 13.4 and 11.7 mA cm^{-2}, respectively. The J_{sc} values calculated from integration of the IPCE spectra are within 5–10%, which conform well to those obtained from the *J–V* measurements, supporting the reliability of the photovoltaic measurement. Regardless of the blend ratios, the data for these devices highlight an important fact in that IPCE exceeds 50% for more than half of the visible region.

Besides the absorption and energy levels, charge-carrier mobility is another crucial factor for achieving high-efficiency devices. Both hole- and electron-mobility were calculated using the space-charge-limited current (SCLC) model at low voltage.[37,38] The device characteristics were extracted by modeling the dark current under forward bias, described by the Mott–Gurney law. We found about threefold enhancement in hole mobility of the 1 : 1 PBDTT-TTFQ:$PC_{71}BM$ devices compared to the 1 : 2 PBDTT-TTFQ:$PC_{71}BM$ devices, with mobility increasing from 2.2×10^{-4} cm^2 V^{-1} s^{-1} to 6.5×10^{-4} cm^2 V^{-1} s^{-1} (see Fig. 4). Moreover, the 1 : 1 device shows a well-balanced mobility ($\mu_e/\mu_h = 1.5$) as compared to that of the 1 : 2 device ($\mu_e/\mu_h = 4.0$). The balanced mobility contributes, in part, to the higher J_{sc} and FF observed in the optimized BHJ devices because the accumulated SCLC charges and hence recombination processes are reduced by the increased hole mobility and enhanced charge collection efficiency.[35,36]

The nano-scale morphology plays an important role in the device performance. Proper morphology is necessary not only for exciton dissociation but also for charge transport to respective electrodes for efficient collection.[32–36] Therefore, the morphological structures of PBDTT-TTFQ:$PC_{71}BM$ blend films with various compositions were probed by tapping mode atom force microscopy (TM-AFM) measurements. In Fig. 5a and d, the pristine film reveals a highly dense fibrillar nanostructure with a certain degree of long-range order, suggesting the nanoscale self-assembly of PBDTT and TTFQ segments (*vide infra*). The distinct spacing of the nanostructures has a lateral dimension ranging from 18 to 22 nm, which is approximately in the same magnitude as the exciton diffusion length, and may effectively assist charge transport prior to recombination.[11] The 1 : 1 PBDTT-TTFQ:$PC_{71}BM$ blend film (Fig. 5b and e) shows a

Table 2 Hole and electron mobility and photovoltaic performance for BHJ devices

D–A ratio	V_{oc} [V]	J_{sc} [mA cm^{-2}]	FF [%]	$PCE_{max/ave}$ [%]	μ_h [cm^2 V^{-1} s^{-1}]	μ_e [cm^2 V^{-1} s^{-1}]	μ_e/μ_h
1 : 1	0.75	14.6	56.1	6.1/6.0	6.5×10^{-4}	1.0×10^{-3}	1.5
1 : 2	0.72	12.8	52.3	4.8/4.6	2.2×10^{-4}	8.9×10^{-4}	4.0

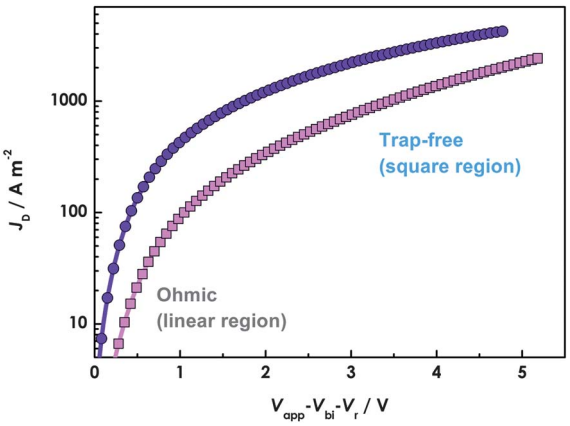

Fig. 4 Determination of the hole mobility from the dark current densities for PBDTT-TTFQ:$PC_{71}BM$ diodes with (●) 1 : 1 and (■) 1 : 2 compositions. The applied voltage was corrected for the built-in voltage (V_{bi}) arising from the work function difference between the contacts and the voltage loss (V_r) due to contact resistance and series resistance across the electrodes.

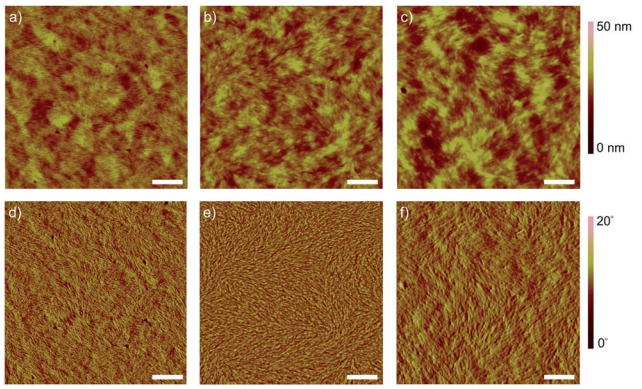

Fig. 5 Morphology characterization of TM-AFM height (upper row) and phase images (lower row) of PBDTT-TTFQ:$PC_{71}BM$ blend films with various compositions: (a and d) 1 : 0, (b and e) 1 : 1, and (c and f) 1 : 2. The imaging area is 3 μm × 3 μm. The scale bar is 500 nm in each panel.

relatively finer and more evenly distributed morphological surface with a root-mean-square (rms) roughness of 3.8 nm, which is beneficial to the exciton dissociation and charge carriers transportation.[33] The 1 : 2 blend film (Fig. 5c and f) shows a similar surface morphology to the 1 : 1 blends, but forms a larger cluster with a rms roughness of 5.2 nm. The net result is to destroy the continuous percolating pathway for hole and electron transport to the corresponding electrodes, thereby increasing the rate of recombination of charge carriers and reducing the V_{oc},[32,36] accounting for the lower PCE (*vide supra*). Moreover, the rough surface will also induce high surface resistance, which is destructive to the performance of solar cells. These results suggest that, 1 : 1 blends may provide an adequate combination of polymer solubility and miscibility with $PC_{71}BM$ to achieve optimal film morphology. The nanoscale phase separation of PBDTT-TTFQ:$PC_{71}BM$ blend films was also examined by TEM experiments. As shown in Fig. S16,† the bright PBDTT-TTFQ-rich domains tend to form a highly dense fibrillar nanostructure, whereas the dark $PC_{71}BM$-rich domains are well distributed in the polymer matrix. The PBDTT-TTFQ nanofibers with 13–20 nm in width are observed in the TEM images. These nanofibers form an interpenetrated network surrounded by the $PC_{71}BM$ phase, the combination of which develops a bicontinuous nanoscale morphology that enlarges the contact area between the PBDTT-TTFQ nanofibers and the $PC_{71}BM$ clusters for efficient charge separation and transport. These TEM images of blend films are identical to those of TM-AFM observations shown in the Fig. 5.

To gain deeper insight into the molecular packing and nanostructural order within the active layer, synchrotron grazing incidence wide-angle X-ray scattering (GIWAXS) analysis was performed to examine the neat polymer film and the optimized 1 : 1 PBDTT-TTFQ:$PC_{71}BM$ BHJ blend film. In Fig. 6a, the 2D GIWAXS pattern of the neat PBDTT-TTFQ film shows arc and anisotropic ring scattering patterns. The Bragg scattering peak of (100) appears relatively strong in intensity at $q = 0.302$ Å^{-1} with an interlayer d_{100} spacing of 20.80 Å, corresponding to the periodic lamellae of polymer backbones, and the weak diffraction peak at $q \sim 0.64$ Å^{-1} represents the second-order (200) reflection of lamellae (d_{200} spacing $\sim$ 9.83 Å). Moreover, the stronger intensity of the (100) reflection in the out-of-plane scattering profile than in the in-plane scattering profile indicated that the lamellar packing PBDTT-TTFQ preferentially stacked out of the film plane (edge-on rich orientation), though with some randomness. The results may be attributed to the introduction of branched alkyl side-chains in PBDTT-TTFQ resulting in the misorientation of the polymer lamellae.[39] In addition, PBDTT-TTFQ homopolymer exhibited a distinctive arc scattering along the q_z axis at $q = 1.75$ Å^{-1}, corresponding to the face-to-face (010) π–π stacking packing reflection peak of the polymer backbones. We also notice that the (010) peak is prominent in the out-of-plane orientation, which implies a large portion of π–π stacking

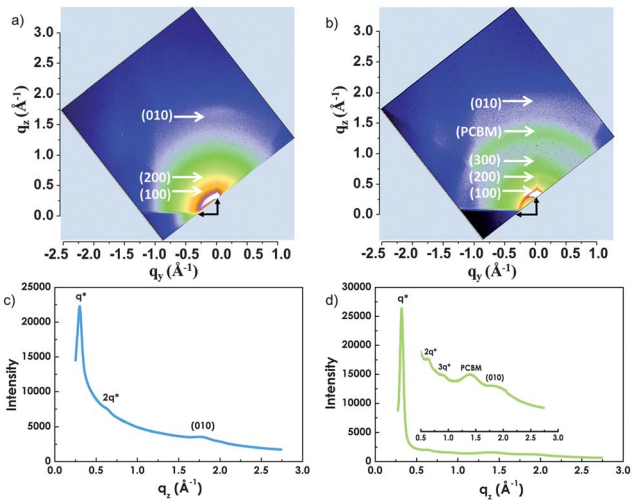

Fig. 6 Two-dimensional grazing incidence X-ray scattering (GIWAXS) patterns of the (a) neat PBDTT-TTFQ film and (b) 1 : 1 PBDTT-TTFQ:$PC_{71}BM$ blend film after thermal annealing at 150 °C for 10 min. GIWAXS out-of-plane diffractograms of the corresponding (c) neat PBDTT-TTFQ film and (d) 1 : 1 PBDTT-TTFQ:$PC_{71}BM$ blend film.

is perpendicular to the substrate. This arrangement is beneficial for charge transport in the device and has often correlated with high OPV performance.[5,23–25] Additionally, the result coincides with the TM-AFM image of the neat PBDTT-TTFQ (Fig. 5a) that clearly reveals a crystalline fibrillar interpenetrating network, possibly owing to the strong intermolecular π–π interactions.[11,40] It is noteworthy that the arc and anisotropic ring scatterings became sharper and more intense than those of the as-cast film (Fig. S17†) upon thermal annealing, suggesting that structures of the film became more ordered and preferentially oriented after thermal annealing. Interestingly, the same diffraction peaks of the pristine polymer were still visible in the 2D patterns of the blend film shown in Fig. 6b. The lamellar packing is visible in the blends, indicating that the PBDTT-TTFQ is able to retain the same edge-on arrangement of the molecules when blended with fullerene. The broad ring is corresponding to the presence of nanoscale $PC_{71}BM$ domains interspersed in the blended phase (Fig. 6b), indicating random orientation with respect to the film substrate. Moreover, in assessing the effect of these π–π interactions on solar cell performance, it is important to consider π-stacking distance. Compared with panels c, d of Fig. 6, the π–π stacking distance in the blend film (d_{010} spacing = 3.26 Å) is significantly smaller than that in the neat film (d_{010} spacing = 3.49 Å). A shorter distance is thought to reduce the energetic barrier for charge hopping between adjacent molecules, which can enhance the out-of-plane charge transport and light absorption, resulting in the increase of device performance.[41,42] An additional intense (300) reflection peak can be clearly observed, indicating that lamellar stacking of the blend film has further been improved (see Fig. 6b and d). The result may arise from the strong polymer–fullerene interactions that delay the fullerene self-assembly in the final drying process. Therefore, fullerene aggregation during film formation may promote the self-organization of the polymer.[43,44]

By extracting from the out-of-plane GIWAXS profile, the 1-D intensity profiles of (100) reflection peak associated with the backbone lamellae of the neat PBDTT-TTFQ, and the PBDTT-TTFQ:$PC_{71}BM$ blend film are plotted in Fig. 7. Gaussian curve fitting results indicate that the full width at half-maximum (FWHM) value for the blend film (0.042 $Å^{-1}$) is significantly smaller than that of the pristine film (0.053 $Å^{-1}$). The smaller FWHM of the scattering patterns corresponds to a larger crystal dimension in the polymer as a result of mixing with $PC_{71}BM$, indicating that fullerene could induce polymer self-assembly towards the kinetics equilibration of the blends' phase separation.[11,45]

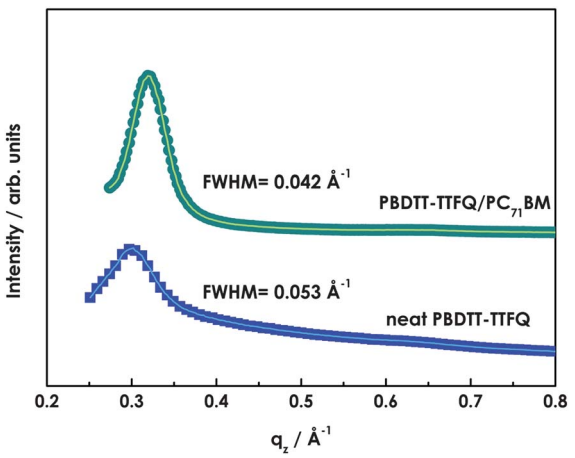

Fig. 7 Overlay of GIWAXS out-of-plane diffractograms of neat PBDTT-TTFQ film and 1 : 1 PBDTT-TTFQ:$PC_{71}BM$ blend film after thermal annealing at 150 °C for 10 min.

Conclusion

In conclusion, a novel PBDTT-TTFQ D–A copolymer with thiophene π-bridge units has been successfully synthesized and characterized. Not only did the resulting copolymer reveal a very broad and intense absorption profile, but it also preserved many attractive properties of the desired deep HOMO and LUMO energy levels, semicrystallinity, high hole mobility, and optimal blending with fullerenes at favorable ratios, allowing high V_{oc} and J_{sc} values. PSCs prepared from 1 : 1 PBDTT-TTFQ:$PC_{71}BM$ blends exhibited a high power conversion efficiency of 6.1% with a short-circuit current density of 14.6 mA cm^{-2}, an open-circuit voltage of 0.75 V, and a fill factor of 56.1% under AM 1.5G illumination, which reveals a promising candidate for next-generation solar cell materials. The results also indicate that the TTFQ unit is an ideal building block to develop high-performance polymer solar cells. Further modifications to the polymer structure and the device architecture are being tested in an effort to achieve better performances.

Notes and references

1 Y. Li, *Acc. Chem. Res.*, 2012, **45**, 723–733.
2 Y.-J. Cheng, S.-H. Yang and C.-S. Hsu, *Chem. Rev.*, 2009, **109**, 5868–5923.
3 H.-C. Chen, Y.-H. Chen, C.-C. Liu, Y.-C. Chien, S.-W. Chou and P.-T. Chou, *Chem. Mater.*, 2012, **24**, 4766–4772.
4 H. Zhou, L. Yang, A. C. Stuart, S. C. Price, S. Liu and W. You, *Angew. Chem., Int. Ed.*, 2011, **50**, 2995–2998.
5 Y. Huang, X. Guo, F. Liu, L. Huo, Y. Chen, T. P. Russell, C. C. Han, Y. Li and J. Hou, *Adv. Mater.*, 2012, **24**, 3383–3389.
6 L. Huo, J. Hou, S. Zhang, H.-Y. Chen and Y. Yang, *Angew. Chem., Int. Ed.*, 2010, **49**, 1500–1503.
7 S. C. Price, A. C. Stuart, L. Yang, H. Zhou and W. You, *J. Am. Chem. Soc.*, 2011, **133**, 4625–4631.
8 T.-Y. Chu, J. Lu, S. Beaupré, Y. Zhang, J.-R. Pouliot, S. Wakim, J. Zhou, M. Leclerc, Z. Li, J. Ding and Y. Tao, *J. Am. Chem. Soc.*, 2011, **133**, 4250–4253.
9 L. Huo, S. Zhang, X. Guo, F. Xu, Y. Li and J. Hou, *Angew. Chem., Int. Ed.*, 2011, **50**, 9697–9702.
10 Z. He, C. Zhong, X. Huang, W.-Y. Wong, H. Wu, L. Chen, S. Su and Y. Cao, *Adv. Mater.*, 2011, **23**, 4636–4643.
11 H.-C. Chen, I.-C. Wu, J.-H. Hung, F.-J. Chen, I.-W. P. Chen, Y.-K. Peng, C.-S. Lin, C.-h. Chen, Y.-J. Sheng, H.-K. Tsao and P.-T. Chou, *Small*, 2011, **7**, 1098–1107.
12 L. Huo and J. Hou, *Polym. Chem.*, 2011, **2**, 2453–2461.

13 H.-C. Chen, S.-W. Chou, W.-H. Tseng, I.-W. P. Chen, C.-C. Liu, C. Liu, C.-L. Liu, C.-h. Chen, C.-I. Wu and P.-T. Chou, *Adv. Funct. Mater.*, 2012, **22**, 3975–3984.
14 A. V. Patil, W.-H. Lee, K. Kim, H. Park, I. N. Kang and S.-H. Lee, *Polym. Chem.*, 2011, **2**, 2907–2916.
15 J.-H. Tsai, W.-Y. Lee, W.-C. Chen, C.-Y. Yu, G.-W. Hwang and C. Ting, *Chem. Mater.*, 2010, **22**, 3290–3299.
16 A. Najari, S. Beaupré, P. Berrouard, Y. Zou, J.-R. Pouliot, C. Lepage-Pérusse and M. Leclerc, *Adv. Funct. Mater.*, 2011, **21**, 718–728.
17 D. Chen, Y. Zhao, C. Zhong, G. Yu, Y. Liu and J. Qin, *Polym. Chem.*, 2011, **2**, 2842–2849.
18 H.-C. Chen, C.-W. Lai, I.-C. Wu, H.-R. Pan, I.-W. P. Chen, Y.-K. Peng, C.-L. Liu, C.-h. Chen and P.-T. Chou, *Adv. Mater.*, 2011, **23**, 5451–5455.
19 H. Zhang, Y. Liu, D. Yao and B. Yang, *Chem. Soc. Rev.*, 2012, **41**, 6066–6088.
20 M. Wright and A. Uddin, *Sol. Energy Mater. Sol. Cells*, 2012, **107**, 87–111.
21 I. Gur, N. A. Fromer, C. P. Chen, A. G. Kanaras and A. P. Alivisatos, *Nano Lett.*, 2007, **7**, 409–414.
22 J.-F. Lin, W.-C. Yen, C.-Y. Chang, Y.-F. Chen and W.-F. Su, *J. Mater. Chem. A*, 2013, **1**, 665–670.
23 P. M. Beaujuge, W. Pisula, H. N. Tsao, S. Ellinger, K. Müllen and J. R. Reynolds, *J. Am. Chem. Soc.*, 2009, **131**, 7514–7515.
24 C. Piliego, T. W. Holcombe, J. D. Douglas, C. H. Woo, P. M. Beaujuge and J. M. J. Fréchet, *J. Am. Chem. Soc.*, 2010, **132**, 7595–7597.
25 L. Ye, S. Zhang, W. Ma, B. Fan, X. Guo, Y. Huang, H. Ade and J. Hou, *Adv. Mater.*, 2012, **24**, 6335–6341.
26 H. Pan, Y. Li, Y. Wu, P. Liu, B. S. Ong, S. Zhu and G. Xu, *Chem. Mater.*, 2006, **18**, 3237–3241.
27 H. Pan, Y. Wu, Y. Li, P. Liu, B. S. Ong, S. Zhu and G. Xu, *Adv. Funct. Mater.*, 2007, **17**, 3574–3579.
28 C. J. Brabec, A. Cravino, D. Meissner, N. S. Sariciftci, T. Fromherz, M. T. Rispens, L. Sanchez and J. C. Hummelen, *Adv. Funct. Mater.*, 2001, **11**, 374–380.
29 J. Peet, J. Y. Kim, N. E. Coates, W. L. Ma, D. Moses, A. J. Heeger and G. C. Bazan, *Nat. Mater.*, 2007, **6**, 497–500.
30 J. K. Lee, W. L. Ma, C. J. Brabec, J. Yuen, J. S. Moon, J. Y. Kim, K. Lee, G. C. Bazan and A. J. Heeger, *J. Am. Chem. Soc.*, 2008, **130**, 3619–3623.
31 B. C. Schroeder, Z. Huang, R. S. Ashraf, J. Smith, P. D'Angelo, S. E. Watkins, T. D. Anthopoulos, J. R. Durrant and I. McCulloch, *Adv. Funct. Mater.*, 2012, **22**, 1663–1670.
32 W. L. Leong, S. R. Cowan and A. J. Heeger, *Adv. Energy Mater.*, 2011, **1**, 517–522.
33 A. Baumann, T. J. Savenije, D. H. K. Murthy, M. Heeney, V. Dyakonov and C. Deibel, *Adv. Funct. Mater.*, 2011, **21**, 1687–1692.
34 H. Zang, Y. Liang, L. Yu and B. Hu, *Adv. Energy Mater.*, 2011, **1**, 923–929.
35 L. J. A. Koster, S. E. Shaheen and J. C. Hummelen, *Adv. Energy Mater.*, 2012, **2**, 1246–1253.
36 R. A. J. Janssen and J. Nelson, *Adv. Mater.*, 2013, **25**, 1847–1858.
37 V. D. Mihailetchi, L. J. A. Koster, P. W. M. Blom, C. Melzer, B. de Boer, J. K. J. van Duren and R. A. J. Janssen, *Adv. Funct. Mater.*, 2005, **15**, 795–801.
38 V. D. Mihailetchi, H. Xie, B. de Boer, L. J. A. Koster and P. W. M. Blom, *Adv. Funct. Mater.*, 2006, **16**, 699–708.
39 I. Osaka, R. Zhang, J. Liu, D.-M. Smilgies, T. Kowalewski and R. D. McCullough, *Chem. Mater.*, 2010, **22**, 4191–4196.
40 Y. Li, S. P. Singh and P. Sonar, *Adv. Mater.*, 2010, **22**, 4862–4866.
41 Y. Kim, S. Cook, S. M. Tuladhar, S. A. Choulis, J. Nelson, J. R. Durrant, D. D. C. Bradley, M. Giles, I. McCulloch, C.-S. Ha and M. Ree, *Nat. Mater.*, 2006, **5**, 197–203.
42 V. Coropceanu, J. Cornil, D. A. da Silva Filho, Y. Olivier, R. Silbey and J.-L. Brédas, *Chem. Rev.*, 2007, **107**, 926–952.
43 B. Schmidt-Hansberg, M. Sanyal, M. F. G. Klein, M. Pfaff, N. Schnabel, S. Jaiser, A. Vorobiev, E. Müller, A. Colsmann, P. Scharfer, D. Gerthsen, U. Lemmer, E. Barrena and W. Schabel, *ACS Nano*, 2011, **5**, 8579–8590.
44 J. Rivnay, S. C. B. Mannsfeld, C. E. Miller, A. Salleo and M. F. Toney, *Chem. Rev.*, 2012, **112**, 5488–5519.
45 A. C. Mayer, M. F. Toney, S. R. Scully, J. Rivnay, C. J. Brabec, M. Scharber, M. Koppe, M. Heeney, I. McCulloch and M. D. McGehee, *Adv. Funct. Mater.*, 2009, **19**, 1173–1179.

